Numerical Investigation of the Three-Dimensional Development in Boundary-Layer Transition

H. F. Fasel*
University of Arizona, Tucson, Arizona
U. Rist† and U. Konzelmann†
University of Stuttgart, Stuttgart, Federal Republic of Germany

A numerical method for solving the complete Navier-Stokes equations for incompressible flows is introduced that is applicable for investigating three-dimensional transition phenomena in a spatially growing boundary layer. Results are discussed for a test case with small three-dimensional disturbances for which detailed comparison to linear stability theory is possible. The validity of our numerical model for investigating nonlinear transition phenomena is demonstrated by realistic spatial simulations of the experiments by Kachanov and Levchenko[1] for a subharmonic resonance breakdown and of the experiments of Klebanoff et al.[2] for a fundamental resonance breakdown.

I. Introduction

WHEN the background turbulence level is very small, the transition process in a flat plate boundary layer is initiated by spatially growing two-dimensional Tollmien-Schlichting waves. This was convincingly demonstrated in the landmark experiments by Schubauer and Skramstad.[3] However, as also observed in their experiments and later documented in great detail in the experiments by Klebanoff et al.,[2] the two-dimensional waves assume a three-dimensional, spanwise-periodic structure as soon as the wave amplitudes reach certain finite amplitudes. At first, it was only conjecture, but today there is sufficient evidence that the development of the spanwise periodicity is a consequence of a secondary instability of the base flow, together with the two-dimensional Tollmien-Schlichting waves.[4,5] The three-dimensional disturbances grow rapidly to large amplitudes and then trigger the breakdown to the random, turbulent motion.

From "controlled" experiments, including laboratory experiments and numerical simulations, two different secondary instability mechanisms could be identified, namely, subharmonic resonance and fundamental resonance. For the case of subharmonic resonance, disturbances arise with twice the period and twice the wavelength of the fundamental Tollmien-Schlichting waves. This was observed in the experiments by Kachanov and Levchenko.[1] The three-dimensional disturbances for the case of fundamental resonance, on the other hand, consist of a time-periodic component and a time-invariant component that has the structure of longitudinal vortex. Both disturbance components have the same wavelength in the spanwise direction and grow rapidly in the downstream direction. This case was investigated in the experiments by Klebanoff et al.[2] Whether the resonance is of the fundamental or subharmonic type depends on the nature of the background disturbances as well as on the amplitude of the two-dimensional Tollmien-Schlichting wave. Roughly speaking, for small amplitudes, the subharmonic resonance appears to dominate, whereas for larger amplitudes, the fundamental resonance prevails. However, this issue is far from resolved, and more detailed investigations are necessary.

Important contributions toward the understanding of the secondary instability mechanisms were made with various theoretical/numerical models.[4-11] However, for simplicity, in all of these models, spatial (x) periodic behavior of the flowfield is assumed. This restriction might not have any negative effect for investigations of the basic instability mechanisms. For more quantitative investigations and even transition predictions, however, the spatial periodicity is probably too much of a restriction. Often, the argument is used that spatially periodic results could be transformed into temporally periodic results with spatial growth (in the downstream direction) using the Gaster[12] transformation. However, this transformation is only valid for small amplification rates, an assumption that is not satisfied for the very large growth rates associated with secondary instabilities.

In this paper, a numerical model is introduced that allows for investigations of spatially growing, three-dimensional disturbance waves in a growing boundary layer. The so-called nonparallel effects are included in the model. Therefore, if successful, our numerical model should be applicable to investigations of the realistic spatial evolution of the secondary instabilities as observed in the laboratory experiments.[1,2]

Toward this end, the numerical method was subjected to several critical tests. The first tests were for linearly growing, small, three-dimensional disturbances. For small amplitudes, our Navier-Stokes results could be validated by comparison to linear stability theory results using the Squire transformation.[13] One typical test calculation is discussed in this paper to demonstrate the applicability of our numerical model for investigating three-dimensional transition phenomena.

Finally, results of simulations of the laboratory experiments by Kachanov and Levchenko[1] and Klebanoff et al.[2] are discussed in detail.

II. Governing Equations and Boundary Conditions

For the numerical method, the Navier-Stokes equations are used in a vorticity transport formulation for the disturbance variables. The vorticity components are denoted by ω_x, ω_y, and ω_z, and u, v, and w are the velocity components of the disturbance flow in the x, y, and z directions, respectively (see Fig. 1). The two-dimensional base flow is represented by the velocity components u_B and v_B in the x and y direction, respectively, and the vorticity in the z direction, ω_{z_B}. Then, the vor-

Presented as Paper 87-1203 at the AIAA 19th Fluid Dynamics, Plasma Dynamics, and Lasers Conference, Honolulu, HI, June 8-10, 1987; received Jan. 25, 1988; revision received Feb. 27, 1989.

*Professor, Aerospace and Mechanical Engineering. Member AIAA.

†Research Assistants, Institut A. Für Mechanik.

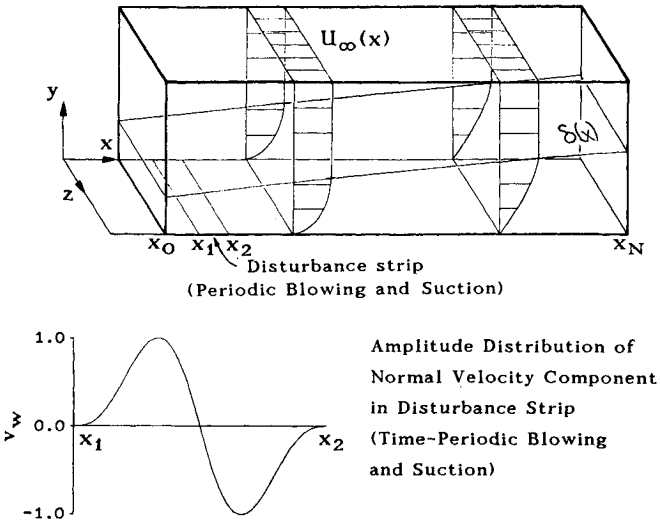

Fig. 1 Integration domain and disturbance generation.

ticity transport equation for the three disturbance vorticity components is

$$\frac{\partial\omega_x}{\partial t}+\frac{\partial}{\partial y}(v\omega_x-u\omega_y+v_B\omega_x-u_B\omega_y)$$
$$-\frac{\partial}{\partial z}(u\omega_z-w\omega_x+u_B\omega_z+u\omega_{zB})=\tilde{\Delta}\omega_x \tag{1a}$$

$$\frac{\partial\omega_y}{\partial t}-\frac{\partial}{\partial x}(v\omega_x-u\omega_y+v_B\omega_x-u_B\omega_y)$$
$$+\frac{\partial}{\partial z}(w\omega_y-v\omega_z-v_B\omega_z-v\omega_{zB})=\tilde{\Delta}\omega_y \tag{1b}$$

$$\frac{\partial\omega_z}{\partial t}+\frac{\partial}{\partial x}(u\omega_z-w\omega_x+u_B\omega_z+u\omega_{z_B})$$
$$-\frac{\partial}{\partial y}(w\omega_y-v\omega_z-v_B\omega_z-v\omega_{z_B})=\tilde{\Delta}\omega_z \tag{1c}$$

with the Laplace operator

$$\tilde{\Delta}=\frac{1}{Re}\frac{\partial^2}{\partial x^2}+\frac{\partial^2}{\partial y^2}+\frac{1}{Re}\frac{\partial^2}{\partial z^2}$$

The Reynolds number is $Re = U_\infty L/\nu$, where U_∞ is the free-stream velocity, L a reference length, and ν the kinematic viscosity. All variables in (1) are dimensionless; they relate to the corresponding dimensional variables as

$$x=\frac{\bar{x}}{L},\quad y=\frac{\bar{y}}{L}\sqrt{Re},\quad z=\frac{\bar{z}}{L},\quad t=\bar{t}\frac{U_\infty}{L}$$
$$u=\frac{\bar{u}}{U_\infty},\quad v=\frac{\bar{v}}{U_\infty}\sqrt{Re},\quad w=\frac{\bar{w}}{U_\infty} \tag{2}$$

The nondimensional vorticity components are

$$\omega_x=\frac{1}{Re}\frac{\partial v}{\partial z}-\frac{\partial w}{\partial y} \tag{3a}$$

$$\omega_y=\frac{\partial w}{\partial x}-\frac{\partial u}{\partial z} \tag{3b}$$

$$\omega_z=\frac{\partial u}{\partial y}-\frac{1}{Re}\frac{\partial v}{\partial x} \tag{3c}$$

From Eq. (3) and the continuity equation,

$$\frac{\partial u}{\partial x}+\frac{\partial v}{\partial y}+\frac{\partial w}{\partial z}=0 \tag{4}$$

three Poisson-type equations for the three velocity components, u, v, and w can be derived

$$\frac{\partial^2 u}{\partial x^2}+\frac{\partial^2 u}{\partial z^2}=-\frac{\partial\omega_y}{\partial z}-\frac{\partial^2 v}{\partial x\partial y} \tag{5a}$$

$$\tilde{\Delta}v=\frac{\partial\omega_x}{\partial z}-\frac{\partial\omega_z}{\partial x} \tag{5b}$$

$$\frac{\partial^2 w}{\partial x^2}+\frac{\partial^2 w}{\partial z^2}=\frac{\partial\omega_y}{\partial x}-\frac{\partial^2 v}{\partial y\partial z} \tag{5c}$$

The numerical method is based on Eqs. (1) and (5) for the three vorticity components and the three velocity components in the x, y, and z directions, respectively. Such a vorticity-velocity formulation was previously applied successfully for investigating the spatial development of two-dimensional Tollmien-Schlichting waves in a flat-plate boundary layer[14] and inplane Poiseuille flow.[15] In contrast to these two-dimensional simulations,[14,15] now the vorticity transport Eqs. (1) are in conservative form. As discussed later, using the vorticity equations in the conservative form resulted in an overall more efficient numerical method when compared to an otherwise equivalent scheme for which the nonconservative form of the vorticity equations is used. For the two-dimensional calculations, on the other hand, there was no advantage to using the conservative formulation and therefore the nonconservative form was used before. A more detailed discussion of the advantages and disadvantages of using a vorticity-velocity formulation, as well as of using the governing equations for the disturbance variables and not for the total variables, is given in Fasel.[16] Since the vorticity-velocity formulation was used successfully for the investigation of two-dimensional stability and transition phenomena in a flat-plate boundary layer,[14] it was also adopted here.

The base flow velocity components, u_B and v_B, and the z vorticity component that are required in Eqs. (1) are obtained by solving the Navier-Stokes equations for two-dimensional, steady, incompressible flow with a vorticity transport equation in conservative form

$$\frac{\partial}{\partial x}(u_B\omega_{z_B})+\frac{\partial}{\partial y}(v_B\omega_{z_B})=\frac{1}{Re}\frac{\partial^2\omega_{z_B}}{\partial x^2}+\frac{\partial^2\omega_{z_B}}{\partial y^2} \tag{6}$$

and the Poisson-type Eqs. (5a) and (5b) with $\partial/\partial z = 0$, $\omega_x = 0$, and $\omega_y = 0$.

Integration Domain

The governing equations are solved in an integration domain (see Fig. 1) extending in the x direction from $x = x_0$ to $x = x_N$, where x_0 is downstream of the leading edge of the flat plate. The integration domain in the y direction extends from $y = 0$ to $y = y_u$ and typically covers several boundary-layer thicknesses. In the spanwise direction, the flow is assumed to be periodic with the domain extending from $z = 0$ to $z = \lambda_z$ (λ_z is the wavelength in the z direction).

Boundary Conditions

The boundary conditions for calculating the base flow from Eqs. (5a), (5b), and (6) are the same as used in our earlier two-dimensional simulations.[14] At the inflow boundary, $x = x_0$, Blasius profiles are used for $u_B(x_0, y)$, $v_B(x_0, y)$, and $\omega_{z_B}(x_0, y)$. At the wall with no-slip conditions, we have

$$u_B(x, 0)=0,\qquad v_B(x, 0)=0 \tag{7a,b}$$

and the wall vorticity is calculated from

$$\left.\frac{\partial\omega_{z_B}}{\partial x}\right|_{x,0}=-\left.\frac{\partial^2 v_B}{\partial y^2}\right|_{x,0} \tag{7c}$$

All the outflow boundary, $x = x_N$, the second derivatives with

respect to x are set to zero

$$\left.\frac{\partial^2 u_B}{\partial x^2}\right|_{x_N,y} = \left.\frac{\partial^2 v_B}{\partial x^2}\right|_{x_N,y} = \left.\frac{\partial^2 \omega_{z_B}}{\partial x^2}\right|_{x_N,y} = 0 \tag{8}$$

Along the freestream boundary, $y = y_u$, the x velocity component u_B is prescribed (thus allowing the imposition of a streamwise pressure gradient)

$$u(x,\ y_u) = f_u(x) \tag{9a}$$

A condition for v_B results from the continuity condition

$$\left.\frac{\partial v_B}{\partial y}\right|_{x,y_u} = -\left.\frac{\partial u_B}{\partial x}\right|_{x,y_u} \tag{9b}$$

In addition, the freestream boundary is to be so far away from the wall that the boundary condition

$$\omega_{z_B}(x,\ y_u) = 0 \tag{9c}$$

is justified.

For the calculation of the three-dimensional unsteady disturbance flow from Eqs. (1) and (5), the boundary conditions are as follows:

At the inflow boundary, all disturbances are assumed to be zero and, therefore, for all disturbance variables, we have

$$f(x_0,\ y,\ z,\ t) = 0 \tag{10}$$

At the wall, no-slip conditions are used

$$u(x,\ 0,\ z,\ t) = 0, \qquad w(x,\ 0,\ z,\ t) = 0 \tag{11a,b}$$

The v velocity component at the wall can be prescribed as a function of x, z, and t

$$v(x,\ 0,\ z,\ t) = f_v(x,\ z,t) \tag{11c}$$

This allows us to introduce localized x, z, and time-dependent disturbances (blowing and suction) into the flowfield. The specific form of $f_v(x,\ z,\ t)$ is discussed in Sec. III. For the three vorticity components at the wall, the following conditions are used:

$$\frac{\partial^2 \omega_x}{\partial x^2} + \frac{\partial^2 \omega_x}{\partial z^2} = -\frac{\partial^2 \omega_y}{\partial y \partial x} + \frac{\partial}{\partial z}\tilde{\Delta} v \tag{11d}$$

$$\omega_y = 0 \tag{11e}$$

$$\frac{\partial \omega_z}{\partial x} = \frac{\partial \omega_x}{\partial z} - \tilde{\Delta} v \tag{11f}$$

Equation (11d) results from the definition of vorticity (3), the continuity condition (4), and conservation of vorticity

$$\frac{\partial \omega_x}{\partial x} + \frac{\partial \omega_y}{\partial y} + \frac{\partial \omega_z}{\partial z} = 0 \tag{12}$$

Equation (11e) results from the definition of ω_y, Eqs. (3b), and Eq. (11f) results from the Poisson equation (5b).

At the outflow boundary, the disturbances are assumed to be periodic in x with the "local" wave number α and, therefore, for each variable, $f = \{u,\ v,\ w,\ \omega_x,\ \omega_y,\ \omega_z\}$

$$\left.\frac{\partial^2 f}{\partial x^2}\right|_{x_N,y,z,t} = -\alpha^2 f(x_N,y,z,t) \tag{13}$$

is used. Here, α is the local "expected" wave number at the outflow boundary. If not known approximately a priori, it can be determined iteratively (see Fasel[17]). These boundary conditions functioned very well for small amplification rates, whereas for large growth rates, difficulties arose that will be discussed later in Sec. IV.

At the freestream boundary, exponential decay of the velocity components is assumed

$$\left.\frac{\partial u}{\partial y}\right|_{x,y_u,z,t} = -\frac{\alpha^*}{\sqrt{Re}}u(x,y_u,z,t) \tag{14a}$$

$$\left.\frac{\partial v}{\partial y}\right|_{x,y_u,z,t} = -\frac{\alpha^*}{\sqrt{Re}}v(x,y_u,z,t) \tag{14b}$$

$$\left.\frac{\partial w}{\partial y}\right|_{x,y_u,z,t} = -\frac{\alpha^*}{\sqrt{Re}}w(x,y_u,z,t) \tag{14c}$$

where α^* is a wave number dependent on x. The choice of α^* will be discussed later in the context of the numerical method. As for the two-dimensional calculations, the freestream boundary is assumed to be far enough from the wall so that

$$\omega_x(x,y_u,z,t) = \omega_y(x,y_u,z,t) = \omega_z(x,y_u,z,t) = 0 \tag{14d}$$

For the spanwise boundaries at $z = 0$ and $z = \lambda_z$, periodicity conditions are employed. Thus, for all variables and their derivatives,

$$f(x,y,0,t) = f(x,y,\lambda_z,t) \tag{15a}$$

$$\left.\frac{\partial f}{\partial z}\right|_{x,y,0,t} = \left.\frac{\partial f}{\partial z}\right|_{x,y,\lambda_z,t} \tag{15b}$$

is enforced.

Numerical Method

The governing Eqs. (1) and (5) are solved numerically. The numerical method that we developed is a combination of finite-difference approximations in the x and y directions and spectral approximations in the z direction. Exploiting the periodic boundary conditions (15), a spectral (Fourier) ansatz

$$f(x,y,z,t) = \sum_{k=-K}^{K} F_k(x,y,t)\cdot e^{ik\gamma z} \tag{16}$$

is used, where $f = \{\omega_x,\ \omega_y,\ \omega_z,\ u,\ v,\ w\}$, and γ is the spanwise wave number $\gamma = 2\pi/\lambda_z$ (λ_z is the spanwise wavelength).

Substituting (16) into (1) and (5) leads to a system of equations for the k^{th} harmonic in a two-dimensional (x, y) domain $(x_0 \le x \le x_N,\ 0 \le y \le y_u)$

$$\frac{\partial \Omega_{x_k}}{\partial t} + X_k - \Delta^* \Omega_{x_k} = 0 \tag{17a}$$

$$\frac{\partial \Omega_{y_k}}{\partial t} + Y_k - \Delta^* \Omega_{y_k} = 0 \tag{17b}$$

$$\frac{\partial \Omega_{z_k}}{\partial t} + Z_k - \Delta^* \Omega_{z_k} = 0 \tag{17c}$$

and

$$\frac{\partial^2 U_k}{\partial x^2} - \gamma^2 k^2 U_k = -i\gamma k \Omega_{y_k} - \frac{\partial^2 V_k}{\partial x \partial y} \tag{18a}$$

$$\Delta^* V_k = i\gamma k \Omega_{x_k} - \frac{\partial \Omega_{z_k}}{\partial x} \tag{18b}$$

$$\frac{\partial^2 W_k}{\partial x^2} - \gamma^2 k^2 W_k = \frac{\partial \Omega_{y_k}}{\partial x} - i\gamma k \frac{\partial V_k}{\partial y} \tag{18c}$$

where X_k, Y_k, and Z_k are the nonlinear coupling terms that result from the spectral approximations and $\Delta^* = 1/Re\ \partial^2/\partial x^2 + \partial^2/\partial y^2 - \gamma^2 k^2/Re$. With this spectral approximation (16), the α^* required in the boundary conditions for the freestream boundary conditions (14) is $\alpha^* = \sqrt{\alpha^2 + \gamma^2 k^2}$.

For discretizing Eqs. (17) and (18), as well as the governing equations for the two-dimensional base flow, finite-difference

approximations of fourth-order accuracy are used in the x and y direction. The time derivatives in Eq. (17) are approximated with three-point backward differences of second-order accuracy. Thus, the method is fully implicit, i.e., all nonlinear terms are evaluated at the most recent time level.

Solution of the Discretized Equation Systems

The systems of equations resulting from the Fourier-spectral and finite-difference approximations are solved by an iterative procedure based on Gauss-Seidel line iteration. The iteration direction is in x, whereas the unknowns on lines parallel to the y coordinate are obtained by a direct method for pentadiagonal coefficient matrices (modified Thomas algorithm). However, iteration is not required for the discretized systems that result from Eqs. (18a) and (18c) for the evaluation of u and w. Rather, these equation systems can be solved directly with the same method for pentadiagonal systems mentioned previously being used.

The nonlinear terms of Eqs. (17) can be evaluated in two different ways: 1) by direct evaluation of these terms in the spectral space or 2) by transformation into the physical space (collocation), followed by subsequent evaluation of the nonlinear terms in the physical space, and finally back transformation into the spectral space; method 2 allows the use of FFT-routines that are highly vectorizable on vector machines and, therefore, makes this method very efficient for $|K|>2$.

However, for the results discussed in this paper, in which the onset of the three-dimensionality in the transition process is of interest, a small number of Fourier modes is sufficient and, therefore, we used method 1. Our calculations have shown that the use of the vorticity equations in conservative form, Eq. (1), reduced the required computation time for the nonlinear terms to approximately one-third when compared to using the nonconservative form.

III. Generation of Disturbances

For the calculations discussed subsequently, the flow is initially undisturbed, that is, only a boundary layer flow over a flat plate is present. This undisturbed flowfield is obtained by numerically solving the Navier-Stokes equation for steady flow as discussed in Sec. II. Thus, when starting the three-dimensional simulations, all perturbation variables U_k, V_k, W_k, Ω_{x_k}, Ω_{y_k}, and Ω_{z_k} are set to zero at $t=0$. Then, for $t>0$, disturbances are introduced into the integration domain through boundary condition (11c). For the results discussed here, the disturbances are introduced by localized blowing and suction within a narrow strip $x_1 \le x \le x_2$ as shown in Fig. 1. For this, the f_v of Eq. (11c) is chosen as

$$f_{v_k} = v_{w_k}(x) \cdot A_k \sqrt{Re}\, \sin(\beta_k t + \theta_k) \quad \text{for} \quad x_1 \le x \le x_2 \tag{19a}$$

and

$$f_{v_k} = 0 \quad \text{for} \quad x_0 \le x < x_1 \quad \text{and} \quad x_2 < x \le x_N \tag{19b}$$

where A_k and θ_k are real constants that can be chosen to adjust the amplitude and phase of the blowing and suction disturbances and β_k is the dimensionless frequency. With $v_w(x)$, the shape of the x distribution of the blowing and suction velocity can be prescribed; a typical shape that was used for the results discussed here is shown in Fig. 1. The width of the suction strip, $x_2 - x_1$, for these calculations was approximately one Tollmien-Schlichting wavelength, and x_1 was located approximately one wavelength downstream of the inflow boundary.

By choosing A_k in Eq. (19a) to be real and constant in time, the disturbance waves evolving in the flowfield are such that u, v, and ω_z are symmetric with respect to the plane $z=0$, whereas w, ω_x, and ω_y are antisymmetric with respect to $z=0$. Therefore, for Eqs. (17) that are complex in general, now only the real parts of U_k, V_k, and Ω_{z_k} and the imaginary parts of W_k, Ω_{x_k} and Ω_{y_k} have to be evaluated and stored.

Generating the disturbances by localized blowing and suction as proposed here has proven to be an efficient method to generate relatively pure, uncontaminated Tollmien-Schlichting waves. This is discussed in more detail in Konzelmann et al.[18] Comparison with earlier calculations in which the disturbances were introduced at the inflow boundary using eigenfunctions of linear stability theory has shown that "clean" Tollmien-Schlichting waves are present already after a very short distance downstream of the blowing and suction strip. However, due to the fact that for the simulations, the disturbances are introduced for $t>0$ into a flow that was, prior to that, steady and undisturbed, the propagating, time-periodic Tollmien-Schlichting waves are preceded by a wave-front that is essentially a wave packet. Of course, the nonlinear behavior of the leading wave packet would be very different from that of pure Tollmien-Schlichting waves. The more complicated developments in this leading wave packet are not considered here, but will be the subject of another detailed investigation.

IV. Numerical Results

The numerical method discussed in Sec. II was first tested extensively with calculations for two- and three-dimensional waves with very small amplitudes. This allowed detailed comparison with linear stability theory and thus provided a thorough check of the numerical method. A typical test case for small amplitudes and the comparison with linear stability theory will be discussed in this paper. To further check the applicability of our numerical method for investigating realistic transition phenomena, numerical simulations of the laboratory experiments by Kachanov and Levchenko[1] for the subharmonic breakdown and by Klebanoff et al.[2] for the fundamental breakdown were attempted. Results and comparison with the measurements are discussed in detail in this paper. For each of the cases presented here, several test calculations with different mesh sizes were performed. These calculations showed that the step sizes used for the results presented here were adequate and that further refinement of the resolution would not significantly change the results.

In all calculations discussed here, the Reynolds number used in the governing equations was $Re = 10^5$, with freestream velocity $U_\infty = 30$ m/s, reference length $L = 0.05$ m, and the kinematic viscosity for air $\nu = 15 \cdot 10^{-6}$ m^2/s. The Reynolds number, based on the displacement thickness δ_1, $Re^* = U_\infty \delta_1/\nu$, is given by $Re^* = 1.720787\sqrt{x \cdot Re}$ for the case without pressure gradients. The frequency parameter F of the linear stability theory is defined as $F = \tilde{\beta}\nu/U_\infty^2 \cdot 10^4$ ($\tilde{\beta}$ dimensional frequency) and is with our parameters $F = \beta \cdot 10^4/Re$.

Linear Test Case

For the linear (small amplitude) test case discussed here, we used $A_k = 0.0001$ and $\theta_k = 0$ (for $k = 0,1$). The integration domain extended from $x_0 = 0.684$ to $x_N = 3.302$ in the x direction and from $y = 0$ to $y_u = 15.65$ in the y direction. In the x direction, 280 intervals were used; in the y direction, 60. In the time direction, 120 intervals were used per period of the disturbance waves. The spectral approximation (16) was truncated at $K = 1$. The disturbances were generated within a strip between $x_1 = 0.908$ and $x_2 = 1.133$ by blowing and suction, as described in Sec. III, with $\beta_k = 10$ ($F = 1.0$). The spanwise wave number was $\gamma = 20$. Seven time periods were computed, and the data of the seventh period were Fourier-analyzed to allow comparison of our Navier-Stokes calculations with the linear stability theory for spatial amplification.

Spatially (in the x direction) amplified disturbances considered in linear stability theory are of the form

$$\psi(x,y,z,t) = \phi(y) e^{i(\alpha x + \gamma z - \beta t)} \tag{20}$$

In Eq. (20), ψ is the complex disturbance stream function and $\phi(y)$ the amplitude distribution. The wave number α is complex, $\alpha = \alpha_r + i\alpha_i$, where α_r is the real wave number in the x

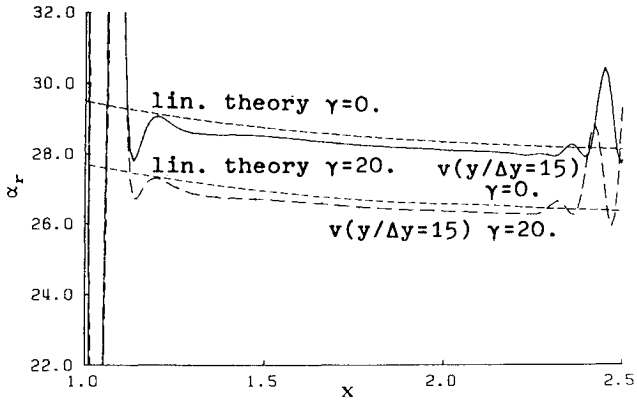

Fig. 2 Comparison of wave number α_r vs x from Navier-Stokes calculations (for v at $y/\Delta y = 15$) with linear stability theory for $\gamma = 0$ and $\gamma = 20$, $\beta = 10$ ($F = 1.0$).

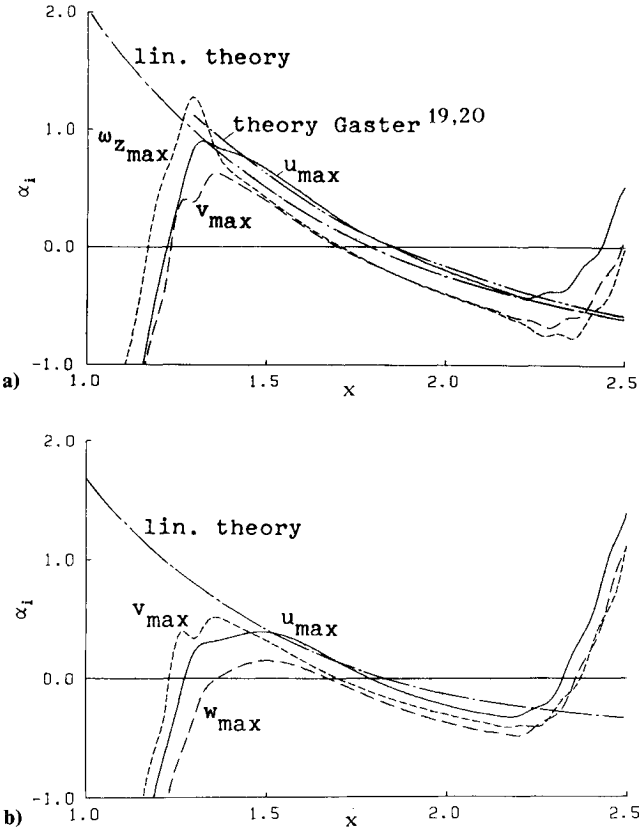

Fig. 3 Comparison of growth rates α_i with linear stability theory for $\beta = 10$ ($F = 1.0$): a) two-dimensional case, $\gamma = 0$ and b) three-dimensional case, $\gamma = 20$.

direction and α_i the growth rate of the disturbances. γ is the wave number in the spanwise (z) direction, and β the dimensionless frequency. Relations analogous to Eq. (20) exist for all other disturbance variables u, v, w, ω_x, ω_y, and ω_z and are used for comparison with the Navier-Stokes calculations.

The disturbance amplitudes A_k were chosen to be small enough so that the nonlinear interactions were truly negligible. Therefore, the disturbance flow can be decomposed into $k = 0$ and $k = 1$ components that then can separately be compared with linear stability theory. The component $k = 0$ corresponds to the two-dimensional wave. The component $k = 1$ corresponds to a three-dimensional disturbance wave. Because of the symmetry with respect to the $z = 0$ plane, the three-dimensional wave component can be interpreted as a superposition of two oblique waves propagating with angles $\theta_+(x) = \tan^{-1}[\gamma/\alpha_r(x)]$ positive in the x and z directions and $\theta_-(x) = \tan^{-1}[-\gamma/\alpha_r(x)]$ positive in the x direction and negative in the z direction.

The comparison of the Navier-Stokes calculations and linear stability theory is documented in Figs. 2–5. Figure 2 shows the wave number α_r for $1.0 \le x \le 2.5$ that was obtained from the normal velocity component v at a constant distance from the wall, $y/\Delta y = 15$. The strong oscillations at the left-hand side for $x < 1.3$ are in the domain where the disturbances are introduced by blowing and suction, and the oscillations at the downstream side are in the domain of the leading wave packet. Comparison with linear stability theory, however, is possible in the central x domain, and it shows that the relative deviation of the Navier-Stokes results from linear stability theory is less than 1% for both the two- and three-dimensional disturbance waves.

A similar comparison is shown in Fig. 3 for α_i, where the α_i of the two-dimensional disturbance wave ($k = 0$) is shown in Fig. 3a and that of the three-dimensional wave ($k = 1$) is given in Fig. 3b. The growth rates were determined at the maxima of the corresponding amplitude distributions. The α_i values exhibit, in all cases, strong growth in the domain where the disturbances are introduced and thus manifest the generation of disturbance waves. Farther downstream, the behavior is governed by linear stability theory, followed again by strong deviations in the domain of the leading wave packet. The growth rates obtained for the Navier-Stokes calculations differ somewhat from the linear stability theory. However, this deviation can be explained by nonparallel effects, that is, the influence of the growing boundary layer. These effects are included in the Navier-Stokes calculations but not in the linear stability theory curves used in Fig. 3. If, for example, for the two-dimensional wave components, our results are compared with curves from the nonparallel theory by Gaster[19,20] then agreement is very good (Fig. 3a).

For the three-dimensional wave components, nonparallel, linear theory results were not available for comparison. To nevertheless demonstrate that the deviations in Fig. 3b and the small deviation is in Fig. 3a were due to nonparallel effects, we used results from a Navier-Stokes calculation for a nongrowing boundary layer for comparison with parallel linear stability theory. Indeed, then these deviations in growth rates α_i, and even the small deviations in α_r, vanish and no longer vary with x.

A comparison of the amplitude distributions for the three-dimensional wave component at $x = 2.0$ is shown in Fig. 4. The amplitude distribution of the Navier-Stokes solution is given in Fig. 4a and of the linear stability theory in Fig. 4b. The corresponding curves of Figs. 4a and 4b essentially collapse and therefore show remarkable agreement between the Navier-Stokes calculations and linear stability theory. The agreement is just as good for the phase relationships with respect to y, as demonstrated when comparing results for the Navier-Stokes calculations (Fig. 5a) and linear stability theory (Fig. 5b). The constant phase difference of $\pi/2$ between the Navier-Stokes solution and linear stability theory for the spanwise velocity component w is due to the fact that only one oblique wave with angle θ_+ is considered in the linear theory whereas two oblique waves with angles θ_+ and θ_- were present in the Navier-Stokes calculation.

Calculation for Subharmonic Resonance

For this calculation, the parameters were chosen such that the laboratory experiments of Kachanov and Levchenko[1] could be simulated. The integration domain extended from $x_0 = 1.427$ to $x_N = 5.742$ in the x direction and from $y = 0$ to $y_u = 20.55$ in the y direction (approximately 3.5 δ at the inflow boundary). We used 934 intervals in the x direction and 60 in the y direction. We calculated 7 time periods of the subharmonic wave component, with 120 intervals per period. The

integration domain extended far enough downstream in the x direction to ensure that a time-periodic state was reached in the x domain of interest (where measurements are available) before the leading wave packet had reached the outflow boundary. For large growth rates that particularly arise in the leading wave packet, the boundary conditions (13) were not satisfactory and caused strong distortions of the flowfield. Therefore, we made sure that results were only used when the leading wave packet had not yet reached the outflow boundary.

The disturbance was introduced at the blowing and suction strip between $1.732 \leq x \leq 2.01$. To achieve subharmonic resonance between two- and three-dimensional disturbances, finite two-dimensional disturbances with $\beta_0 = 12.4$ ($F = 1.24$), $A_0 = 0.00145$, $\theta_0 = 0$, and three-dimensional disturbances with the subharmonic frequency $\beta_1 = 1/2\ \beta_0 = 6.2$ ($F = 0.62$), $A_1 = 6 \times 10^{-6}$, $\theta_1 = 0$ were introduced. The spanwise wave number was $\gamma = 31.47$. For this calculation, the spectral approximations were truncated at $K = 2$. The time-dependent phase difference between the subharmonic and fundamental disturbance that was present in the laboratory experiments was not modeled in our simulations. Otherwise, our calculations closely model the experiments. Here, the two- and three-dimensional disturbance components are denoted as modes (n, k) where n stands for the frequency as the multiples of the fundamental frequency and k denotes the multiples of the spanwise wave number. For example, the two-dimensional fundamental wave is denoted as mode (1, 0) and the three-dimensional subharmonic is denoted as mode (1/2, 1).

Results of these calculations are shown in Figs. 6–10. The results discussed here are from a Fourier analysis of the seventh time period after the disturbance generation was initiated at the blowing and suction strip. Figure 6 shows the spatial development of typical wave components for the u disturbance. The results are presented semilogarithmically, as are the experimental measurements.[1] Also, as in the experiments, the growth curves are for a constant normalized distance from the wall, $y/\delta = 0.26$. For comparison, the experimental measurements are also shown in the same plot; the open circles stand for $k = 0$ and the solid black circles represent $k = 1$. As for the experiments, modes (1, 0) and (1/2, 1) grow rapidly to finite amplitudes. The nonlinearly generated modes (2, 0) and (3/2, 1), on the other hand, grow after some downstream delay. Generally, agreement with the experiments is remarkable. The growth curves start to deviate somewhat toward the downstream end of the integration domain, where the experimental amplification rates are somewhat smaller than those of the Navier–Stokes calculations. This, however, is not surprising since, in this calculation with $K = 2$, we allowed only the first and second harmonic component in z. Therefore, nonlinear interactions with higher harmonic components ($k \geq 3$) are excluded. In addition, in the x domain where the experimental subharmonic mode (1/2, 1) grows more slowly than the numerical one, our calculations exhibit a strong growth of modes (1, 2) and (2, 2) with wave number $k = 2$. On one hand, these wave components influence (dependent on the z location) the measurement of modes (1, 0) and (2, 0) and, on the other hand, they influence the other modes by nonlinear interaction. To investigate this influence in more detail, we intend to make another calculation with a larger x domain.

Amplitude and phase distributions with respect to y of the numerical simulation and experiments are compared in Figs. 7–9 for $x = 3.709$. To demonstrate the remarkable quantitative agreement between simulations and experiment, for the comparison of the amplitude profiles for u in Figs. 7a and 8, the curves were not normalized by the u maxima. In contrast, in Fig. 9a, the u amplitude was normalized by its inner maximum. The amplitude and phase distributions for the funda-

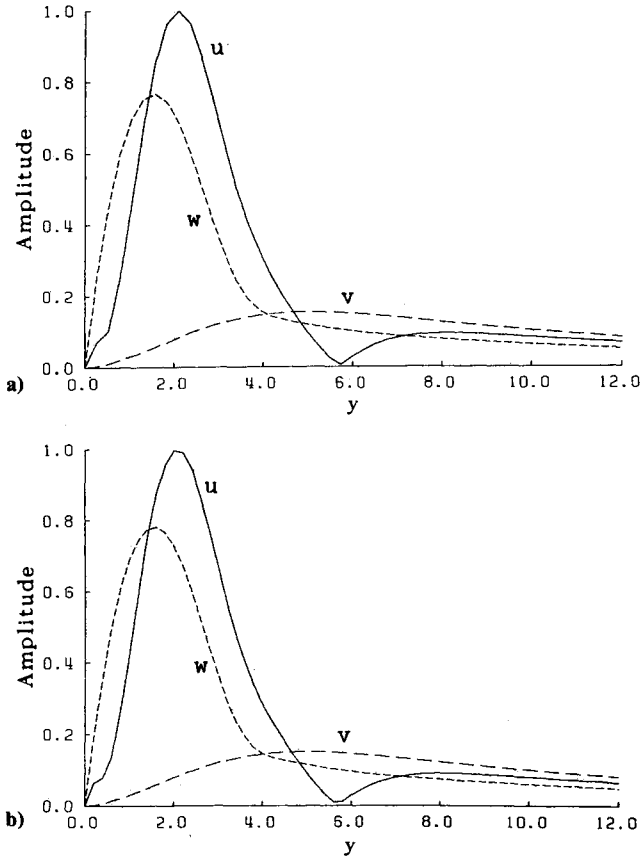

Fig. 4 Comparison of amplitude distributions for the three disturbance velocity components u, v, w with linear stability theory at $x = 2.0$ ($Re^* = 770$), $\beta = 10$ ($F = 1.0$), $\gamma = 20$: a) Navier-Stokes solution and b) linear stability theory.

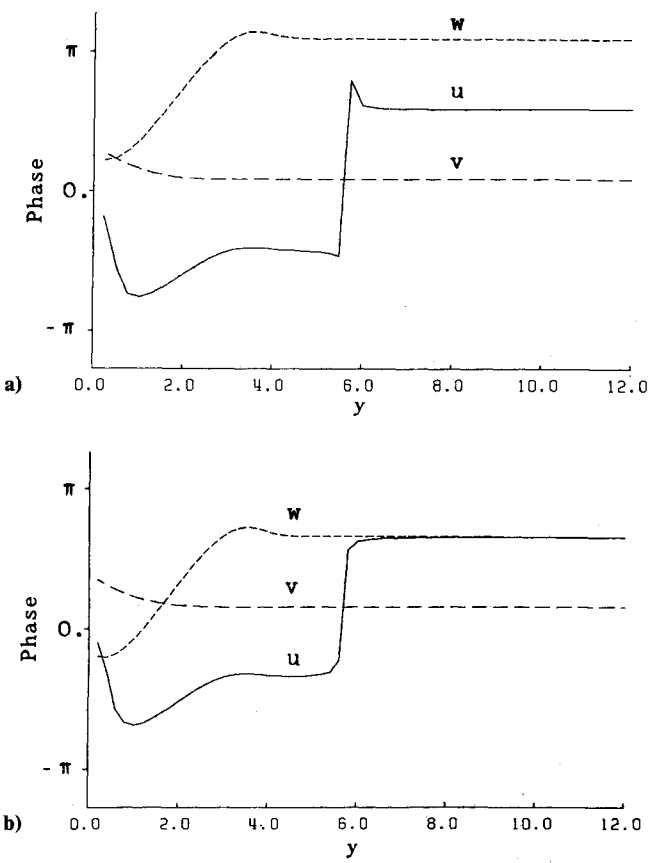

Fig. 5 Comparison of the phase distribution for the three velocity components u, v, w with linear stability theory at $x = 2.0$ ($Re^* = 770$), $\beta = 10$ ($F = 1.0$), $\gamma = 20$: a) Navier-Stokes solution and b) linear stability theory.

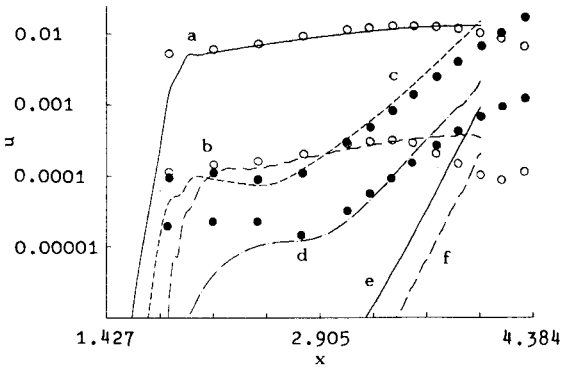

Fig. 6 Compariosn of amplification curves with measurements by Kachanov and Levchenko[1] for various wave components. Circles and dots are measurements; lines are Navier-Stokes solutions.
a = mode (1. 0) fundamental second mode; d = mode (3/2, 1);
b = mode (2, 0) second higher harmonic; e = mode (1, 2);
c = mode (1/2, 1) subharmonic; f = mode (2, 2).

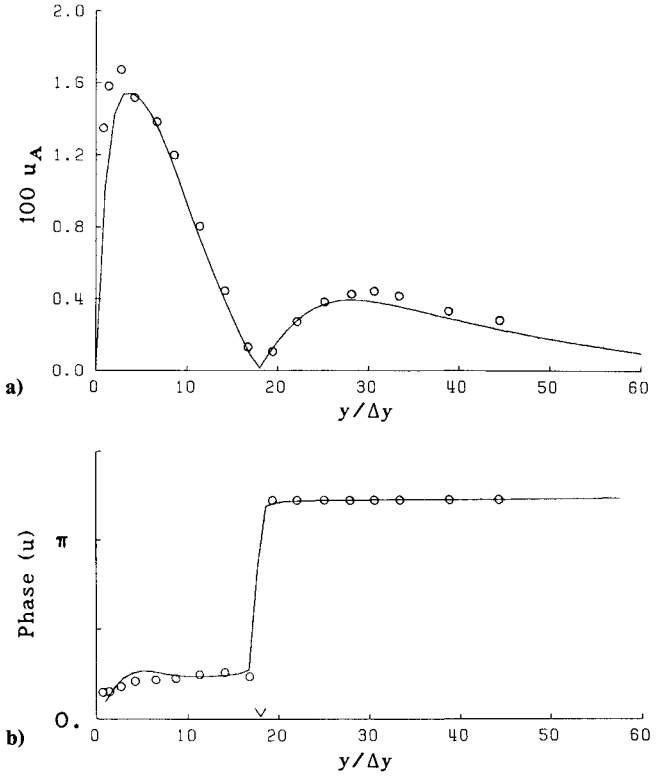

Fig. 7 Amplitude and phase distribution of the two-dimensional fundamental component [mode (1, 0)] at $x = 3.709$ ($Re^* = 1048$). Circles are measurements by Kachanov and Levchenko,[1] lines are Navier-Stokes solutions: a) amplitude and b) phase.

mental mode (1, 0) are shown in Fig. 7. Except for the slight deviation close to the inner maximum for the u amplitude, the agreement between simulation and experiment, in particular for the phase, is very good. The amplitude profiles for various three-dimensional wave components are shown in Fig. 8. Considering the very small amplitudes of modes (3/2, 1) and (5/2, 1) of approximately 0.03 and 0.005% (relative to the free-stream velocity), respectively, and considering the experimental difficulties in reliably measuring such small fluctuations, the agreement between experiment and simulation in Figs. 8b and 8c is indeed remarkable. The normalized amplitude distribution and phase distribution for the subharmonic mode (1/2, 1) in Fig. 9 almost perfectly matches those obtained experimentally.

In Fig. 10, finally, the amplitude and phase distribution of the nonlinearly generated, strongly amplified wave compo-

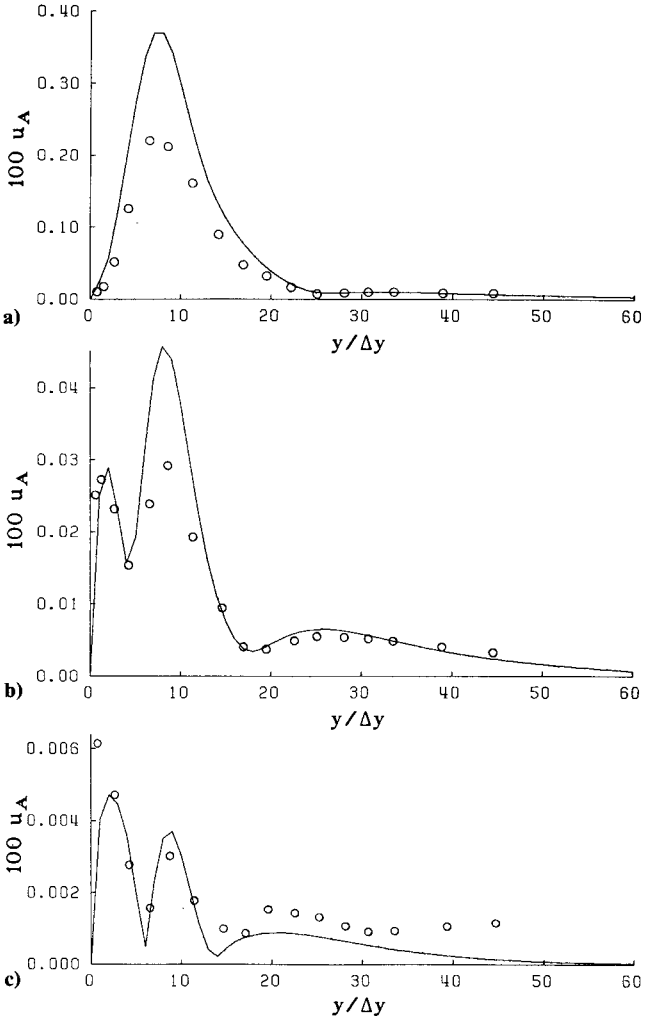

Fig. 8 Amplitude distributions of the three-dimensional wave components ($x = 3.709$, $Re^* = 1048$). Circles are measurements by Kachanov and Levchenko,[1] lines are Navier-Stokes solutions: a) for mode (1/2, 1); b) for mode (3/2, 1); and c) for mode (5/2, 1).

nents with the fundamental frequency and $k = 2$ [mode (1, 2)] are given. For this, measurements were not available.

Calculation for Fundamental Resonance

In contrast to the calculations discussed in the previous section, the frequencies for both the two- and three-dimensional disturbances introduced at the blowing and suction strip were now the same, $\beta = 5.88$ ($F = 0.588$); 1100 intervals were used in the x direction, 72 in the y direction, and $K = 2$. All parameters for this calculation were chosen to match the conditions of the experiments of Klebanoff et al.[2] In order to achieve this, a number of test cases were required because some of the experimental conditions were not known in the detail required. For example, preliminary calculations have shown that by including a time-invariant, spanwise-periodic three-dimensional disturbance, the coupling between the three-dimensional wave component and the two-dimensional one is strongly accelerated. The addition of such a perturbation leads to stationary modulation of the base flow, beginning at the blowing and suction strip, whereas otherwise, such a modulation would only occur farther downstream. A similar modulation of the base flow was possibly present in the experiments of Klebanoff et al.[2] In these experiments, pieces of thin plastic tape were attached to the flat plate in a spanwise-periodic fashion (directly under the vibrating ribbon). However, the variation of the base flow caused by the tape was too small to be measurable.

In Fig. 11, the amplification curves obtained from a numerical simulation that included such a stationary spanwise modulation are shown for a "peak" and "valley" station. Comparison with the measurement by Klebanoff et al.[2] indicates that there is considerable deviation between simulation and experiment, in particular, farther downstream. Calculations, without the spanwise modulation that were attempted previously, demonstrated similar disagreement and, therefore, we had hoped that spanwise modulation would improve the situation. In all cases that we tried, the experimental growth rates were considerably stronger than those calculated. However, indications are that the cause for this disagreement is not due to different physical mechanisms, but rather to the fact that in the experiment the amplification rates for the two-dimensional Tollmien–Schlichting waves are already larger than those of linear stability theory obtained from our two-dimensional Navier-Stokes calculations. This ambiguity was also addressed by Herbert,[5] who suggested "adjusting" the position of the leading edge of the flat plate in his theoretical model.

On the other hand, we conjectured that the discrepancy could be caused by a pressure gradient, although very small, in the experiments. Therefore, we repeated the simulations with small adverse pressure gradients. A small, constant adverse pressure gradient ($\partial p/\partial x = 0.004$, which is a decrease of the freestream u velocity of about 1% per x unit length) yields an amplification curve for the two-dimensional Tollmien–Schlichting waves that closely matches that of Klebanoff et al.,[2] as shown in Fig. 12. The strong influence of the pressure gradient becomes obvious when comparison of this amplification curve is made with that for a zero pressure gradient, as presented in Fig. 12.

In Fig. 13, the amplification curves at the peak and valley stations are plotted for calculations with the same constant pressure gradient that approximately reproduced the experimental amplification curves as shown in Fig. 12. When com-

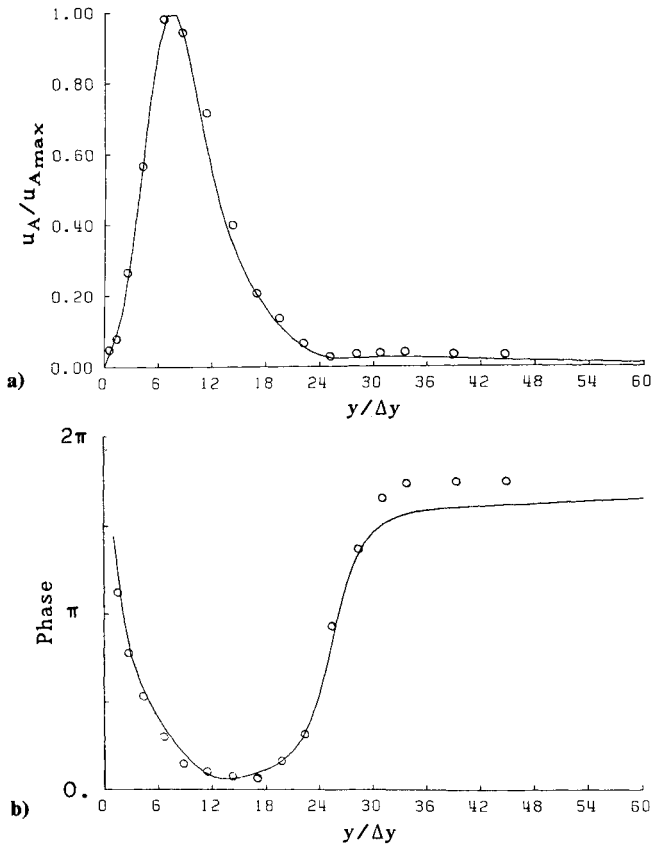

Fig. 9 Amplitude and phase distribution for subharmonic mode (1/2, 1) at $x = 3.709$ ($Re^* = 1048$). Circles are measurements by Kachanov and Levchenko,[1] lines are Navier-Stokes solutions: a) amplitude and b) phase.

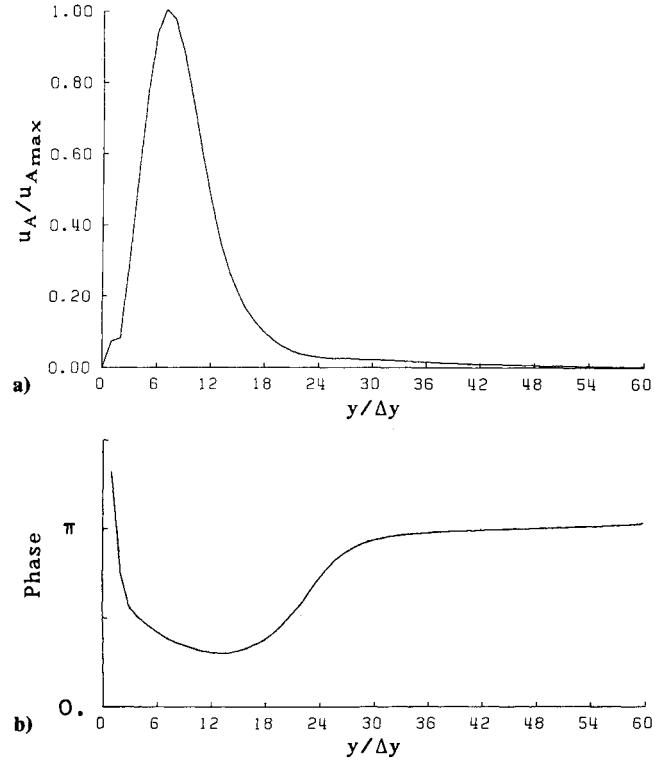

Fig. 10 Amplitude and phase distributions of the three-dimensional mode (1, 2) at $x = 3.709$ ($Re^* = 1048$): a) amplitude and b) phase.

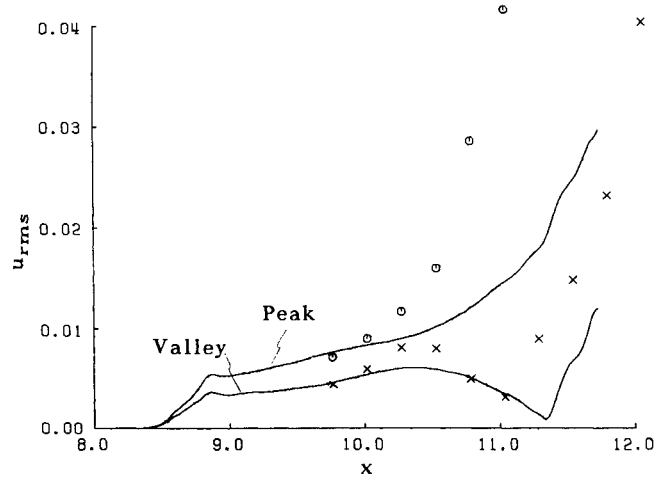

Fig. 11 Amplification curves (rms of the total u disturbances) at the peak and valley positions (zero pressure gradient).
o = measurements at peak position;
× = measurements at valley position[2];
—— = Navier-Stokes solutions.

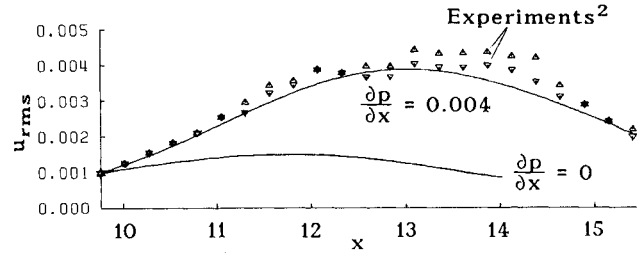

Fig. 12 Amplification curves for two-dimensional disturbances of small amplitudes for a zero pressure gradient and a small adverse pressure gradient ($\partial p/\partial x = 0.004$) (from u disturbance component at $y/\Delta y = 7$). Comparison with measurements by Klebanoff et al.[2]

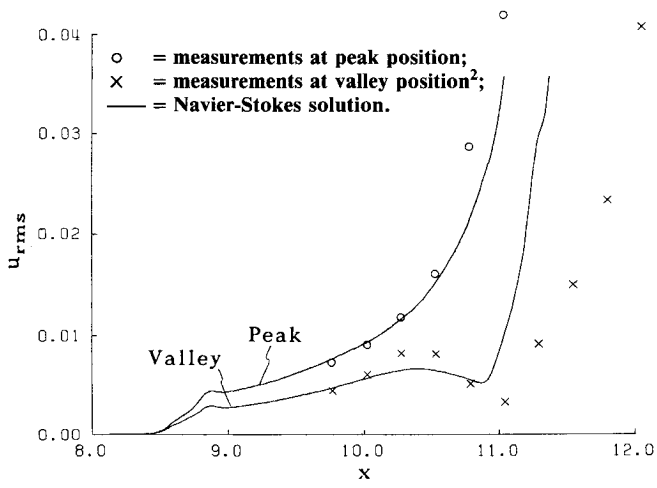

Fig. 13 Amplification curves (rms of the total u disturbance) at peak and valley positions for small adverse pressure gradient ($\partial p/\partial x = 0.004$).

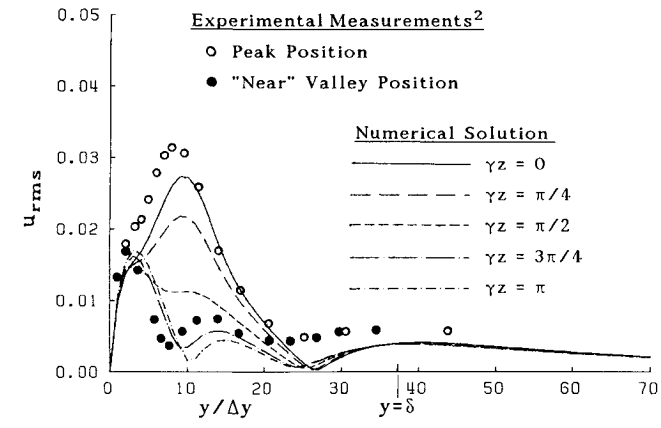

Fig. 14 Amplitude distributions of rms of total u disturbance at $x = 10.91$ for various z positions. Comparison with measurements[2] at peak position ($\gamma z = 0$) and at "near" valley position (between $\gamma z = 3\pi/4$ and $\gamma z = \pi$).

paring these growth curves with the corresponding ones in Fig. 11, the effect of a small pressure gradient becomes quite obvious. The growth rates are now much bigger and agreement with experiments is much better. With better matching of the pressure gradient and/or using more spanwise modes, possibly even better agreement could be achieved. Finally, the rms amplitudes at $x = 10.91$ and various spanwise positions are also plotted in Fig. 14. Comparison with corresponding measurements for a peak ($\gamma z = 0$) and a "near" valley ($\gamma z \cong 3/4\pi$) station shows good qualitative agreement.

V. Conclusions

In this paper, we introduced a numerical method for solving the complete Navier-Stokes equations for incompressible flows that is applicable to investigations of transition phenomena in a spatially growing boundary layer. The model is "spatial," that is, the disturbance waves grow or decay in the downstream direction in contrast to the development in time that occurs for the "temporal" model.

Test calculations for small amplitudes have shown very good agreement with linear stability theory and the nonparallel theory of Gaster,[19] where effects of the growing boundary layer were included in the analysis. A simulation of the experiments by Kachanov and Levchenko[1] for the subharmonic breakdown convincingly demonstrated that the spatial development can be realistically modeled with our numerical method. In particular, the nonlinearly generated harmonic wave components and their development in the downstream direction can be correctly calculated, both qualitatively and quantitatively.

Simulations of the experiments by Klebanoff et. al.[2] showed poor agreement of the spatial growth of the disturbances at peak and valley stations. However, when introducing a small pressure gradient, such that the small-amplitude (linear) growth of a two-dimensional Tollmien-Schlichting wave was similar to that measured in the experiments, the amplification curves for peak and valley stations agreed much better with the experiment. This suggests that a small pressure gradient might have been present in the experiments of Klebanoff et al.[2]

These calculations demonstrate that the numerical method is well suited for investigating transition for spatially varying mean flows. We are now in a position to apply this numerical method to the investigation of some of the many still open questions of laminar-turbulent transition.

Acknowledgments

This research is the result of an international cooperation between the University of Stuttgart and the University of Arizona. Funding was provided by the Deutsche Forschungsgemeinschaft and the Office of Naval Research.

References

[1]Kachanov, Y. S. and Levchenko, V. Y., "The Resonant Interaction of Disturbances at Laminar-Turbulent Transition in a Boundary Layer," *Journal of Fluid Mechanics,* Vol. 138, 1984, pp. 209-247.

[2]Klebanoff, P. S., Tidstrom, K. D., and Sargent, L. M., "The Three-Dimemsional Nature of Boundary-Layer Instability," *Journal of Fluid Mechanics,* Vol. 12, 1962, pp. 1-34.

[3]Schubauer, G. B. and Skramstad, H. K., "Laminar Boundary Layer Oscillations and Stability of Laminar Flow," NBS Res. Paper 1772, Washington, D.C., 1943.

[4]Orszag, S. A. and Patera, A. T., "Secondary Instability of Wall-Bounded Shear Flows," *Journal of Fluid Mechanics,* Vol. 128, 1983, pp. 347-385.

[5]Herbert, T., "Three-Dimensional Phenomena in the Transitional Flat-Plat Boundary Layer," AIAA Paper 85-0489, 1985.

[6]Benney, D. J. and Lin, C. C., "On the Secondary Motion Induced by Oscillations in a Shear Flow," *Physics of Fluids,* Vol. 3, 1960, pp. 656-657.

[7]Craik, A. D. D., "Non-Linear Resonant Instability in Boundary Layers," *Journal of Fluid Mechanics,* Vol. 50, 1971, pp. 393-413.

[8]Herbert, T., "Analysis of the Subharmonic Route to Transition in Boundary Layers," AIAA Paper 84-0009, 1984.

[9]Wray, A. and Hussaini, M. Y., "Numerical Experiments in Boundary-Layer Stability," *Proceedings of Royal Society of London,* Vol. A392, 1984, pp. 373-389.

[10]Spalart, P. R., "Numerical Simulation of Boundary-Layer Transition," *Springer Lecture Notes in Physics,* Vol. 218, 1985, pp. 531-535.

[11]Kleiser, L. and Laurien, E., "Numerical Investigation of Interactive Transition Control," AIAA Paper 85-0566, 1985.

[12]Gaster, M., "A Note on the Relation Between Temporally-Increasing and Spatially-Increasing Disturbances In Hydrodynamic Stability," *Journal of Fluid Mechanics,* Vol. 14, 1962, pp. 222-224.

[13]Squire, H. B., "On the Stability of Three-Dimensional Disturbances of Viscous Fluid Between Parallel Walls," *Proceedings of Royal Society of London,* Vol. A142, 1933, pp. 621-628.

[14]Fasel, H, "Investigation of the Stability of Boundary Layers by a Finite-Difference Model of the Navier-Stokes Equations," *Journal of Fluid Mechanics,* Vol. 78, 1976, pp. 355-383.

[15]Fasel, H. and Bestek, H., "Investigation of Nonlinear, Spatial Disturbance Amplification in Plane Poiseuille Flow," *Proceedings of IUTAM Symposium on Laminar-Turbulent Transition,* Springer-Verlag, New York, 1980.

[16]Fasel, H., "Recent Developments in the Numerical Solution of the Navier-Stokes Equations and Hydrodynamic Stability Problems, Lecture Notes," *VKI-Lecture Series on Computational Fluid Dynamics,* Hemisphere Corp., 1978.

[17]Fasel, H., "Untersuchungen zum Problem des Grenzschichtumschlages durch Numerische Integration der Navier-Stokes-Gleichungen," Dissertation, Univ. of Stuttgart, FRG, 1974.

[18]Konzelmann, U., Rist, U., and Fasel, H., "Erzeugung Dreidimensionaler, Räumlich Angefachter Störwellen Durch Periodisches Ausblasen und Absaugen in einer Plattengrenzschichtströmung," *ZAMM Z. Angew. Math. Mech.,* Vol. 67, 1987, pp. 298-300.

[19]Gaster, M., "On the Effects of Boundary-Layer Growth on Flow Stability," *Journal of Fluid Mechanics,* Vol. 66, 1974, pp. 465-480.

[20]Gaster, M., private communication, 1986.